Microphysical properties of various precipitation systems worldwide classified via objective methods based on dual-frequency precipitation radar observations

Yujia Zhang[1,2] Xiaodong Zhang[1,2], Xiang Ni[1,2]

[1]Chongqing Jinfo Mountain Karst Ecosystem National Observation and Research Station, School of Geographical Sciences, Southwest University, Chongqing, China
[2]Chongqing Engineering Research Center for Remote Sensing Big Data Application, School of Geographical Sciences, Southwest University, Chongqing, China

Correspondence to: Xiang Ni (nixiang@swu.edu.cn)

Abstract. Microphysical properties play crucial roles in physical processes related to the development of precipitation. In this study, Global Precipitation Measurement (GPM) dual-frequency precipitation radar (DPR) data were processed to demonstrate the microphysical properties of different precipitation systems (PS) that are objectively classified with the k-means clustering algorithm. Four types of regular/non-extreme PS (high-latitude shallow PS, subtropical shallow PS, moderate PS, deep PS) and four types of extreme PS (extreme deep PS, strong PS, extreme strong PS, and marine extreme PS) were recognized. These eight types of PS exhibit differences in spatial-temporal features and convection characteristics, such as storm height, rain intensity, and vertical structures. For example, the extreme strong PS, with the highest radar echo top and largest mean mass-weighted mean diameter are mainly located over tropical continents, whereas high-latitude shallow PS have the least precipitation rate and mean normalized intercept parameter values. The relationships between convection features and microphysical properties also vary among the eight types of PS. For extreme PS, maximum precipitation rate near the surface generally exceeds 100 mm h^{-1} and balanced breakup and coalescence processes play a dominant role compared with non-extreme PS. In contrast, the coalescence processes dominate near the surface in two types of shallow PS. These results highlight the diversity of global precipitation microphysics and emphasize the necessity of global studies to increase the understanding of precipitation processes.

1. Introduction

The microphysical characteristics of precipitation provide crucial information for describing precipitation. The deficiency of precipitation microphysical parameterization schemes is a significant factor contributing to precipitation errors in weather and climate models (Snook and Xue, 2008). Accurately obtaining spatiotemporal variations in precipitation microphysical parameters is essential for understanding the physical processes of precipitation, increasing the accuracy of quantitative precipitation estimation, and evaluating microphysical parameterizations in models (Chen et al., 2011; Zhang et al., 2023). Currently, observations and characteristics of precipitation microphysics at the global scale remain lacking because of the limited number of observation approaches.

The drop size distribution (DSD) is a typical metric for depicting precipitation microphysics. DSD features can be derived from observations obtained via disdrometers, ground-based radar instruments, and space-based radar instruments. In radar instruments, the interaction of electromagnetic waves with hydrometeors is used to retrieve DSD parameters (Marzuki et al., 2023), whereas disdrometers measure raindrop counts to directly obtain DSDs at the surface. Disdrometers provide only point measurements at specific levels and cannot measure the vertical structure of DSDs. Moreover, disdrometer observations are relatively sparse, especially over the ocean. Although ground-based radar instruments can measure the three-dimensional structure of precipitation, they can only be used in limited areas, and their observation accuracy is significantly affected by the terrain conditions within the observation area (Dai et al., 2020). In contrast, space-based radar instruments can provide the vertical structures of DSD parameters worldwide. This study focuses on the microphysical characteristics of various precipitation systems (PS) worldwide. Compared with other instruments, space-based radar instruments are the most suitable for researching global precipitation microphysics.

In 1997, the Tropical Rainfall Measuring Mission (TRMM) satellite was launched by the National Aeronautics and Space Administration (NASA) and the Japan Aerospace Exploration Agency (JAXA). The precipitation radar (PR), which operates in the Ku-band (13.8 GHz), was carried by the TRMM (Iguchi et al., 2000). This marked the beginning of the observation of precipitation microphysics via space-based radar instruments. In 2014, NASA and JAXA successfully launched the Global Precipitation Measurement (GPM) Core Observatory (GPM-CO). The GPM-CO carried the first spaceborne dual-frequency precipitation radar (DPR) system, operating in the Ku and Ka bands (13.6 and 35.5 GHz, respectively) (Skofronick-Jackson et al., 2017). Via the use of this characteristic, mean mass-weighted mean diameter (D_m) and mean normalized intercept parameter (N_w) can be retrieved. The retrieved DSD parameters have been verified with ground-based observations and exhibit closer agreement with in situ measurements than those derived from the TRMM PR algorithm (Sun et al., 2020). In addition, validation studies have confirmed the feasibility of using DPR observations for DSD parameter analysis (D'Adderio et al., 2018; Peinó et al., 2024). Peinó et al. (2024) used observational data from seven Parsivel disdrometers across different topographic zones in the western Mediterranean to validate GPM DSD products. They reported that the GPM DPR products

effectively captured the variations in DSDs observed under different rainfall intensities. Therefore, GPM DSD products have been widely employed to investigate the microphysical characteristics of precipitation in the literature (Wen et al., 2024, 2023) .

However, previous studies involving GPM DSD products have focused mainly on specific locations or weather systems. For example, Li et al. (2024) studied the vertical structure and DSD characteristics of different precipitation types during the rainy season over South China and reported that the precipitation type and intensity affect the DSD parameters. In their study, under the same precipitation intensity, shallow convective precipitation exhibited the smallest D_m and largest N_w values, whereas deep convective precipitation exhibited the opposite phenomenon. Additionally, regarding stratiform precipitation, for precipitation rate > 3.5 mm h^{-1}, D_m slightly increased, and in regard to shallow convective precipitation, D_m remained at approximately 1.3 mm for Precipitation Rate > 2 mm h^{-1}. Similarly, Wen et al. (2023) analyzed the seasonal variations in the vertical structure of precipitation microphysics in East China. They reported that the spatial distributions of D_m and N_w demonstrated obvious seasonal variations and that there are more small raindrops in convective precipitation in autumn and winter than during the other seasons. Additionally, regarding weather conditions, regional variations in the precipitation characteristics of tropical cyclones have been investigated over the North Indian Ocean (Kumar et al., 2023). Research has revealed that the nature of microphysical processes largely influences the growth of droplets in convective and stratiform rain. Wu et al. (2022) investigated the DSD characteristics of record-breaking Typhoon In-Fa. Their findings revealed significant internal and regional differences in the microphysical characteristics of typhoon precipitation. When different precipitation types during Typhoon In-Fa were compared, convective precipitation (N_w values ranging from 3.80 to 3.96 m^{-3} mm^{-1}) exhibited higher raindrop concentrations than did stratiform precipitation (N_w values ranging from 3.40 to 3.50 m^{-3} mm^{-1}). Additionally, convective precipitation during Typhoon In-Fa indicated a greater (lower) raindrop concentration than that during Typhoon Taiwan (Hainan), while the raindrop diameter was smaller than those during both Typhoons Taiwan and Hainan. These studies primarily focused on the microphysical process and structure of various weather conditions, which provided insight into the formation process of precipitation.

At present, there are few studies on the microphysical characteristics of large-scale and global PS. On the one hand, as mentioned above, the DSD is influenced by numerous factors, such as precipitation type and season. There may be multiple precipitation types and DSDs in one area. On the other hand, few DSD datasets covering the whole world are available. Dolan et al. (2018) used twelve disdrometer datasets across three latitudinal zones—high-latitude, midlatitude, and low-latitude zones—to analyze DSD spatial variability. They reported that the DSD varies with latitude. At low latitudes, moderate D_m values (1.5–2 mm) and large log10(N_w) values (> 4 m^{-3} mm^{-1}) dominated. At midlatitudes, high D_m values and small N_w values dominated. At high latitudes, low D_m and large N_w values prevailed. The twelve disdrometers mainly located in the United States, Darwin, Finland, and central Indian ocean, and hence it failed to capture precipitation microphysical characteristics over all climatic regimes. Hence, in this study, GPM DSD products were employed to investigate the microphysical characteristics of PS at global scales.

This study aims to objectively classify PS based on DPR observations using a machine learning approach and to systematically analyze the microphysical characteristics of the resulting PS types. By constructing a unified, data-driven classification framework, the results help clarify regional variability in drop size distributions (DSDs) and provide new insight into the microphysical processes governing different precipitation regimes. This study is organized in four sections. Section 2 provides detailed descriptions of the GPM data and machine learning models applied in this study. The main results are presented in Section 3, and finally, a summary is given in Section 4.

2. Data and methods

2.1. Data

GPM observations cover the range from 65° S to 65° N (Hou et al., 2014; Tapiador et al., 2012). The GPM DPR operates in the Ka and Ku bands, with a spatial resolution of approximately 5×5 km^2. The scanning of DPR is cross-track and has three scan patterns: normal scan, matching scan, and high sensitivity scan (Das et al., 2022). Since the scanning pattern of the Ka-band was changed in 2018 (Awaka et al., 2021), the GPM 2A DPR (version 7) products considered the changes in the Ka-band scan pattern with a more accurate precipitation estimation algorithm. The product formats in version 7 have been changed from the original three types to two types: Full scan and High Sensitivity scan. The Full scan product exhibits a new format and is defined as a full-scan dual-frequency product with a 125-m vertical range resolution. Compared with previous algorithms, the FS mode makes it possible for the first time to process a full-scan band of approximately 245 km in dual-band mode (Awaka et al., 2021). Therefore, the observations from the Full scan were adopted in this study.

In this study, five years (2018–2022) of 2A DPR products (version 7) were employed. The parameters used in this machine learning model are showed in Table1. Detailed descriptions of the generation and retrieval of these parameters can be found in Iguchi et al. (2021). The microphysical variables analyzed here are directly taken from the standard GPM DPR products. Previous studies have extensively evaluated the GPM DPR products on a global scale (Chase et al., 2020; Gatlin et al., 2020; Huang et al., 2022; Peinó et al., 2024; Seela et al., 2023), supporting their suitability for scientific analyses. The precipitation type helps distinguish between stratiform and convective precipitation pixels, while air temperature is used to separate snow from rain. To more strictly exclude potential solid or mixed-phase cases at the surface, this study additionally applies a surface air temperature threshold (>10 °C) when identifying rain-dominated precipitation systems.

Table1. Summary of the input variables used in the machine learning model, including the original DPR variable names, descriptions, and units.

Variable name	Long name	Unit

D_m	mass-weighted mean diameter	mm
N_w	normalized intercept parameter	mm^{-1} m^{-3}
Z_e	reflectivity	dBZ
Zsurf	near-surface reflectivity	dBZ
typeprecip	precipitation type (stratiform/convective)	-
airTemperature	air temperature	K
precipRateNearSurface	near-surface precipitation rate	$mm\ h^{-1}$

123

124 **2.2. Precipitation system (PS)**

125 This paper presents a method based on the connected domain principle for identifying PS, similar to those contained in the
126 widely used TRMM/GPM Precipitation Feature dataset (Liu et al., 2008, 2020). First, pixels with precipitation no less than
127 0.1 mm h^{-1} are derived from DPR orbit data. Then, neighboring precipitation pixels, including diagonally adjacent precipitation
128 pixels, are grouped together as a PS. Each PS is required to have a minimum of four precipitation pixels.
129
130 The DPR provides three-dimensional structure of precipitation and DPR products include radar reflectivity parameters and
131 retrieved DSD parameters from 0 to 22 km with a range resolution of 125 m. Consequently, for each PS type, DSD and radar
132 reflectivity parameters such as the maximum and average values of each layer were calculated. The average D_m and N_w profiles
133 were used for each PS, and when referring to the maximum D_m and N_w values in each layer, MAX-D_m and MAX-N_w were
134 used, respectively. Given the potential relationships of the convective intensity with microphysical parameters, Z_e in the
135 product was employed to calculate several convection indicators. These include the maximum 20/30/40 dBZ echo top height
136 (MAXHT20/30/40) for each type of PS (Liu, 2011; Liu et al., 2020; Ni et al., 2019; Roy et al., 2020), the echo top height of
137 the PS (H_{top}) (Arulraj and Barros, 2021), and other convective parameters. To describe PS conditions, several additional
138 features were calculated, including the maximum precipitation rate near the surface (maximum precipitation rate of the
139 precipitation pixels included in the PS) and precipitation area (the number of precipitation pixels contained in the PS). For the
140 stratiform, convective, land, and oceanic percentages, the corresponding pixel fractions among each individual PS were first
141 calculated. These fractions were then averaged across all PS within a given cluster to represent the cluster-level characteristics.
142 Considering that the GPM satellite exhibits a higher observation frequency in high-latitude regions (approximately 2–3 times
143 that at the equator), the original dataset is prone to oversampling in these areas, which can introduce bias. To construct a
144 balanced dataset suitable for clustering analysis, this study implemented a homogenization for the sampling. Specifically, the
145 satellite's observation frequency was calculated as a function of latitude, and sample size for each latitude was adjusted using
146 the ratio of its frequency to that at the equator. Subsequently, precipitation systems were randomly selected from each latitude

to ensure a consistent scaled sample size, thereby effectively addressing the issue of uneven sampling. Finally, a total of 8,924,307 PS were obtained for subsequent analysis.

2.3. Methods

In this study, two distinct machine learning models, namely k-means clustering and principal component analysis (PCA) were used. Both models were trained and evaluated via the Python scikit-learn package. These models are briefly described below. The k-means algorithm is a widely used unsupervised clustering method in machine learning because of its simplicity and computational efficiency (Jain, 2010). The algorithm follows a three-step process. Initially, it aims to select initial cluster centers by randomly obtaining sample coordinates from the dataset and assigning each sample to its nearest cluster center. Next, it computes the mean of all sample points assigned to each previous cluster center to establish new cluster centers. Finally, the algorithm aims to evaluate the differences between the new and old cluster centers. If differences are present, the last two steps are repeated until the cluster centers stabilize and no longer shift (Jain, 2010).

PCA is a classical dimensionality reduction tool in machine learning (Gang and Bajwa, 2022). PCA is based on the linear combination of target features to construct the principal subspace, and the variance is then employed to measure the information content with the aim of identifying the linear subspace with the maximum variance (Marukatat, 2023). In summary, PCA aims to transform numerous irrelevant features into a comparatively limited number of pertinent ones, thereby retaining as much of the informational content of the original data as possible (Gang and Bajwa, 2022). In our case, we used PCA to reduce the v dimension, compressing the original 176 height levels into a single representative component for each variable (Ze, Dm, or Nw). Vertically integrated variables (e.g., total water path) are not used here, because while they have clear physical meaning, they aggregate information across the vertical column and may obscure important vertical contrasts relevant to precipitation processes. Only one principal component per variable was retained for each profile, as this sufficiently captures the dominant variance of the vertical structure and served as a compact descriptor for clustering (Festa et al., 2023; Jolliffe and Cadima, 2016). The PCA was applied once, independently, for each parameter. Time was not treated as an input dimension; only the vertical (height) dimension was reduced.

In this study, all the ~9 million PS derived in section 2.2 are used. Input parameters of each PS for k-means clustering include the maximum precipitation rate near the surface, the echo top height of the PS, the precipitation area, the proportion of stratiform precipitation, the proportion of convective precipitation, the DSD parameters (D_m and N_w), the maximum Z_e, and the first principal component score of the vertical profiles of Z_e, D_m, and N_w. These parameters were selected based on their critical role in comprehensively characterizing the features, structure, and microphysical processes of precipitation systems. Among them, the maximum surface precipitation rate and Z_e reflect the intensity of the precipitation process and its echo characteristics, while the precipitation area directly characterizes the spatial differences in the horizontal distributions of the system. The H_{top} not only reveals the vertical distribution but also captures the top-level information of the precipitation cloud

through the maximum reflectivity height. Introducing the proportions of stratiform and convective precipitation facilitates the differentiation of precipitation types generated by distinct mechanisms, thereby elucidating their evolution patterns and dynamic characteristics. Furthermore, the DSD parameters (D_m and N_w) effectively describe the size distribution of precipitation particles and their intrinsic physical processes, providing an essential basis for an in-depth understanding of precipitation microphysics.

The quality of clustering was evaluated by analyzing different clustering structures derived from the same dataset. Common clustering performance metrics include the sum of squared errors (SSE), Davis Bouldin (DB) index, Calinski-Harabasz (CH) Score (El Khattabi et al., 2024) and silhouette index, which are widely used to evaluate clustering effectiveness and quality (Ay et al., 2023). In this case, the DB index was calculated by computing the average sum of the intraclass distances between any two clusters divided by the distance between the centers of those two clusters and obtaining the maximum value. The DB index can manage clusters of different sizes and densities with a high degree of robustness to noise and outliers. A lower DB index indicates better clustering performance (Sowan et al., 2023). Additionally, the CH score, which assesses clustering compactness and separation, was also considered. Higher CH scores indicates better-defined clusters. Algorithms with clustering numbers ranging from 3 to 20 were executed, and the resulting change in the DB index and CH score was plotted (refer to Fig. S1 in the Supplementary Material). As shown in Fig. S1, when K = 8, the DB index reaches its minimum while the CH index remains at a relatively high level. This indicates that the clustering at K = 8 achieves a favorable balance between intra-cluster compactness and inter-cluster separation, supporting the selection of eight clusters as an appropriate classification. Although the CH index reaches its maximum at K = 11, the improvement compared with K = 8 is marginal. A comprehensive comparison suggests that using 11 clusters would likely introduce unnecessary redundancy without substantially improving clustering performance. Therefore, based on the combined evaluation of multiple clustering validity metrics, this study ultimately classifies the precipitation systems into eight categories.

3. Results and discussion

3.1. Global distributions

After clustering, each cluster was characterized by its unique precipitation and spatial distribution characteristics, including D_m, MAXHT20/30/40, and convective/stratiform fractions. Table 2 summarizes the statistics of various parameters for the eight types of PS, while Figure 1 illustrates their spatial distributions. For clarity in the subsequent discussion, Clusters 1–8 were grouped and named based on their spatial distributions (Fig. 1) and key precipitation characteristics (Table 2). Four non-extreme precipitation systems were identified (high-latitude shallow, subtropical shallow, moderate, and deep PS), along with four extreme precipitation systems (extreme deep, strong, extreme strong, and marine extreme PS). Overall, extreme precipitation systems account for a smaller proportion and exhibit higher MAXHT20/30/40, larger D_m, and stronger precipitation rates compared with non-extreme precipitation systems. Geographically, high-latitude shallow PS are

predominantly found poleward of 40°N and 35°S, whereas subtropical shallow PS mainly occur within approximately 20° of the equator. The marine extreme convection type is primarily distributed over oceanic regions.

The numbers in Table 2 include abundant information and verify the rationality of the objectively clustering algorithm. First, the numbers of the various types of PS differed significantly. The two types of shallow PS (high-latitude shallow PS and subtropical shallow PS) accounted for 81.44% of the total PS count. The proportions of deep and moderate PS were 2.41% and 15.50%, respectively. The other four types of PS are regarded as extreme PS (extreme deep PS, strong PS, extreme strong PS, and marine extreme PS) because they exhibit markedly stronger precipitation intensity (as shown in Figures 4–6) and vertical development than the other categories and occur very infrequently in the global sample, accounting for only 0.39%, 0.22%, 0.02%, and 0.01% of the total PS, respectively. In the non-extreme PS, MAXHT20 is generally positively related to the precipitation rate (Table 2). However, in the extreme PS, the correlation between the extreme precipitation rate and MAXHT20 is not clear. For example, that the mean value of the maximum precipitation rate in marine extreme PS was the highest among the eight types of PS, although its MAXHT20 was less than that in extreme strong PS and close to that in extreme deep PS. This result is consistent with other studies noting a weak link between the heaviest rainfall and the highest storm top (Hamada et al., 2015). Although the convective intensity of extreme deep PS is not significantly higher than that of deep PS, it exhibits a substantially larger precipitation area and maximum precipitation rate.

High-latitude shallow PS was most prevalent at midlatitudes and high latitudes, where snowfall and sleeting are more frequent than at low latitudes. Notably, high-latitude shallow PS were dominated by stratiform precipitation, with stratiform pixels accounting for 88.63%. Meanwhile, approximately 86.60% of the PS exhibited surface temperatures higher than 0 °C. A study confirmed that at high latitudes and in polar regions, more than 25% of precipitation falls as snow (Lerber et al., 2018). This is consistent with the observations from high-latitude shallow PS. Additionally, an analysis of high-latitude shallow PS by latitude revealed that with increasing latitude, the number of samples generally increased. Moreover, the number of PS with echo top heights less than 2.5 km increased with latitude. During the winter season at 65°S, PS with echo top heights below 2.5 km accounted for approximately 50% of the total PS there. This is likely due to the influence of the low surface temperature and weak convection (refer to Fig. S2 in the Supplementary Material).

Subtropical shallow PS primarily occurred over the ocean dominated by the subtropical high, with a relatively limited degree of overlap with moderate PS and deep PS (Fig. 1). The mean MAXHT20 value in subtropical shallow PS was only 3.29 km, and the proportion of convective precipitation was the highest among all the types of PS, exceeding 90%. Compared with those of the other PS, subtropical shallow PS exhibited the smallest precipitation area. Moreover, it was rarely found over land. These results support the conclusion that subtropical shallow PS is associated with isolated shallow convection over the ocean, which has been the topic of interest in previous studies (Chen and Liu, 2016; Chudler et al., 2022; Houze Jr. et al., 2015).

The geographic distribution patterns of deep PS and moderate PS were approximately the same (Fig. 1). The number of occurrences in the maritime continent (MC), Indian Ocean, Atlantic Ocean, Amazon rainforests and Pacific Ocean were relatively high. These regions are generally influenced by the Intertropical Convergence Zone (ITCZ). Nevertheless, the deep PS has higher land percentage. The mean values of the maximum precipitation rates in moderate PS and deep PS were 6.21, 35.94 mm h^{-1}, respectively, whereas those of MAXHT20 were 7.03 and 11.89 km, respectively. As a result, the spatial distribution of deep PS is very similar to that of the deep convection core (Ni et al., 2019), which is defined as MAXHT20 larger than 10 km.

Strong PS, extreme deep PS, extreme strong PS, and marine extreme PS demonstrated low sample sizes. However, their precipitation areas are significantly larger than non-extreme PS (Table 2). The location of extreme deep PS is similar with moderate and deep PS, with larger values for most parameters. In the extreme strong PS, the proportion of land pixels reaches 81%, with significant concentrations in near-equatorial Africa, America, India, the southeastern U.S., and South America. The average maximum precipitation rate in extreme strong PS was 156.37 mm h^{-1}, and MAXHT40 reached 12.32 km, which is the highest among all the types of PS. The high MAXHT40 value indicates strong updraft in the middle troposphere, which is a hallmark of intense convection and favors hail formation (Kumar et al., 2023; Zipser et al., 2006). Therefore, the spatial distributions of hailstorms in extreme strong PS were very similar to those of the global hail map derived from spaceborne precipitation radar (Ni et al., 2017) and passive microwave sensor (Bang and Cecil, 2021). Marine extreme PS were primarily situated in the near-equatorial marine region, with only 943 PS, of which 90% were over the ocean . The mean maximum precipitation rate in marine extreme PS was 178.30 mm h^{-1}, ranking first among the eight types of PS. Although the MAXHT20 value in marine extreme PS reached 12.81 km, the MAXHT40 value in marine extreme PS was approximately half of that in extreme strong PS, indicating low convection activity in the middle and upper levels. This is consistent with the findings of Liu et al. (2007), who observed that the difference between cloud-top height and MAXHT20 over land is smaller than that over the ocean, indicating that convective intensity is stronger over land than over the ocean.

Oceanic extreme PS (extreme deep PS with a high fraction of ocean pixels and marine extreme PS) have mean precipitation coverage areas exceeding 36000 km2, significantly larger than continental extreme PS (strong PS and extreme strong PS). This spatial distribution aligns with previous findings that the most extensive precipitation systems are predominantly located in oceanic regions according to the study of Zhang and Wang (2021). Furthermore, continental extreme PS display markedly stronger convective intensity. This disparity is largely attributable to the observation that the heaviest PS generally occur over tropical land, the Western Pacific warm pool, the North American Great Plains, and Argentina, whereas the most intense convective storms are predominantly observed over continental areas (Liu and Zipser, 2015).

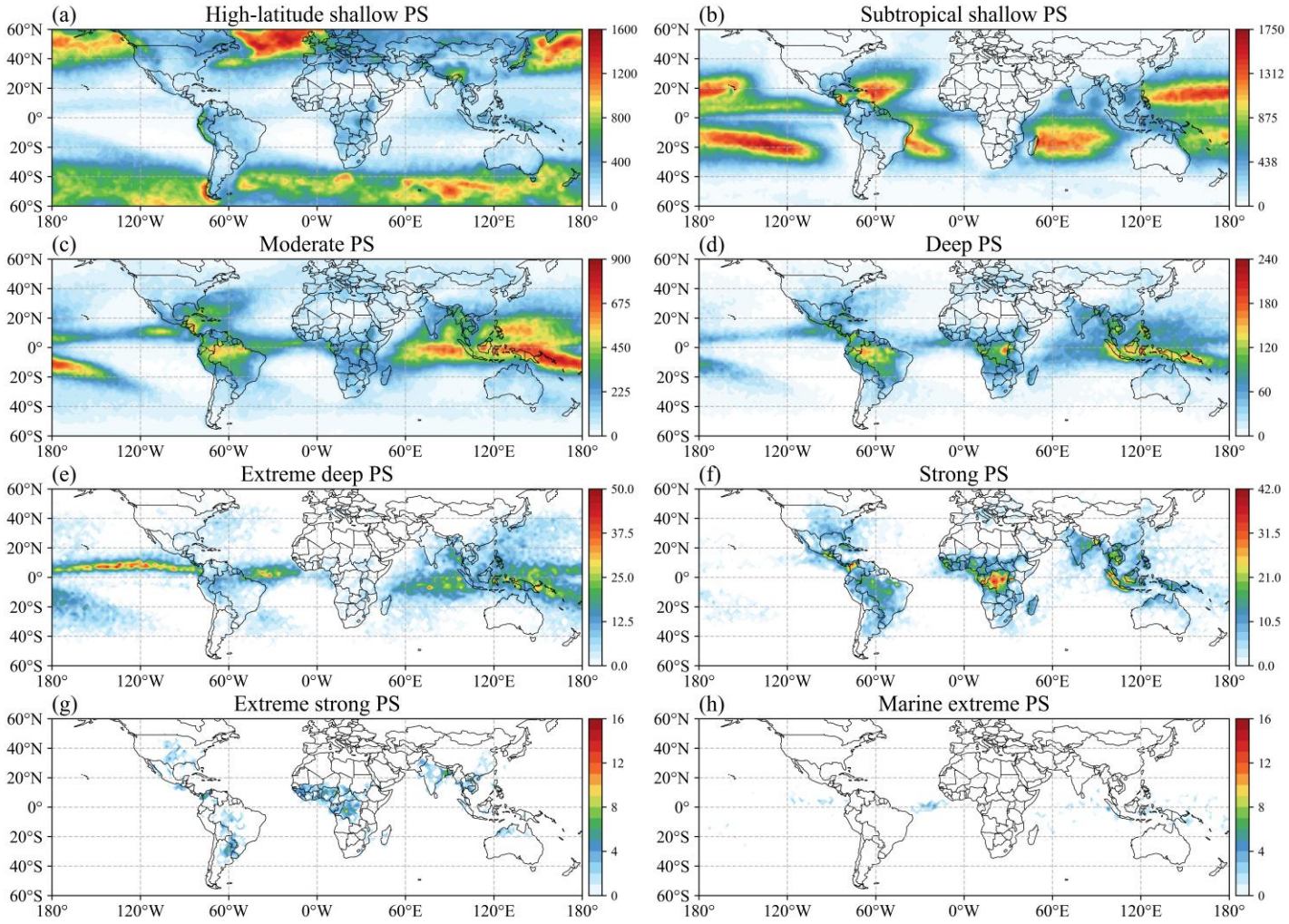

278

279 **Figure 1.** Spatial distributions (2° × 2°) of the PS counts from 2018 to 2022.

280

Table 2. Precipitation parameters for the different types of PS. (* indicate that in high-latitude shallow PS and subtropical shallow PS, approximately 80% of the samples do not reach 40 dBZ. Therefore, the mean MAXHT40 for these samples is recorded as 0.)

	high-latitude shallow	subtropical shallow	Moderate	deep	extreme deep	strong	extreme strong	marine extreme
Mean MAXHT20 (km)	3.40	3.29	7.03	11.89	12.67	15.39	17.21	12.85
Mean MAXHT30 (km)	2.63	2.67	5.11	8.65	8.52	13.68	16.31	9.18
Mean MAXHT40 (km)	0.00*	0.00*	3.44	5.53	5.71	8.64	12.32	6.04
Stratiform percentages (%)	88.63	9.46	54.38	53.22	69.90	57.42	53.02	66.83
Convective percentages (%)	5.85	89.95	42.83	44.52	28.16	39.91	44.06	31.56
Land percentages (%)	21.61	6.97	27.96	42.31	15.61	65.37	80.98	10.45
Ocean percentages (%)	78.39	93.03	72.04	57.69	84.39	34.63	19.02	89.55
Mean precipitation (mm h^{-1})	1.60	2.35	6.21	35.94	156.67	135.46	156.37	178.30
precipitation Standard deviation (mm h^{-1})	1.63	1.92	8.89	50.44	98.44	106.95	103.50	98.61
Number of samples	4,184,547	3,083,077	1,383,261	215,611	34,982	19,790	2,096	943
Mean precipitation area (km^2)	610.57	239.23	2761.46	7009.37	37076.93	18485.91	22521.51	36044.11
>273.15 K frequency (%)	86.60	99.16	99.83	99.97	99.97	99.99	99.99	100.00
2.5 km Mean MAX-log10(N_w) [m^{-3} mm^{-1}]	3.47	3.70	4.06	4.49	5.20	4.72	4.88	6.07
2.5 km Mean MAX-D_m [mm]	1.03	1.17	2.26	2.82	2.71	3.04	3.11	2.61
2.5 km Mean log10(N_w) [m^{-3} mm^{-1}]	3.23	3.45	3.36	3.39	3.83	3.36	3.35	4.45
2.5 km Mean D_m [mm]	0.85	0.89	1.36	1.50	1.30	1.61	1.71	1.32

3.2. Global distributions of microphysical features

Fig. 2 and Fig. 3 show the global distributions of the microphysical parameters for the eight types of PS. To avoid the influence of ground clutter, in each PS, the mean D_m and N_w values at 2.5 km above the ground surface were analyzed. Notably, there was a significant degree of spatial heterogeneity in each panel. The general conclusion is that continental PS exhibit a higher D_m than do oceanic PS. Usually, continental rainfall is associated with high convective activity in which clouds produce large

raindrops. In contrast, oceanic rainfall is accompanied by the formation of weak updrafts and the development of a low melting layer, which impedes the formation of large raindrops and results in a high concentration of small raindrops (Saha et al., 2022; Seela et al., 2018). Moreover, D_m decreases with increasing latitude, a trend that is especially notable in high-latitude marine regions (refer to Fig. S2c in the Supplementary Material). Cha et al. (2021) noted that snow primarily comprises small particles (diameter < 1 mm). In high-latitude shallow PS, snowfall may become more frequent from the middle to high latitudes, which can result in a decrease in D_m. Notably, the height and thickness of the melting layer may influence raindrop growth (Hu et al., 2024). With increasing latitude, the melting layer becomes thinner, thus reducing the conditions necessary for raindrop growth, which may lead to the formation of a larger number of small raindrops. In the oceanic regions within subtropical shallow PS, the higher sea surface temperature in the tropics is more conducive to convection formation and development. Moreover, D_m varies among the eight clusters in a specific region. For example, in the Amazon region, moderate PS exhibits a lower D_m than deep PS does.

Similar to D_m, there is a distinct contrast in N_w between continents and oceans (Das and Chatterjee, 2018). Continental rainfall is usually associated with the cold rain mechanism, whereby raindrops grow as ice particles (Gupta et al., 2023). In contrast, oceanic rainfall is associated with a warm rain regime, in which raindrops grow via a collision-agglomeration mechanism. Consequently, N_w over land is less than that over oceans (Suh et al., 2016). For the same PS, N_w is high in areas with small D_m values and conversely low in areas with large D_m values. For example, in extreme deep PS, the D_m value over the eastern near-equatorial Pacific Ocean, which reaches approximately 1.18 mm, is smaller than that of the other oceanic regions. However, N_w is significantly greater than those in the other regions. In strong PS, the D_m values in near-equatorial Africa and the eastern United States are greater than those in other regions, but the N_w values are lower than those in other regions. It is possible that D_m and N_w may be negatively correlated for the same PS.

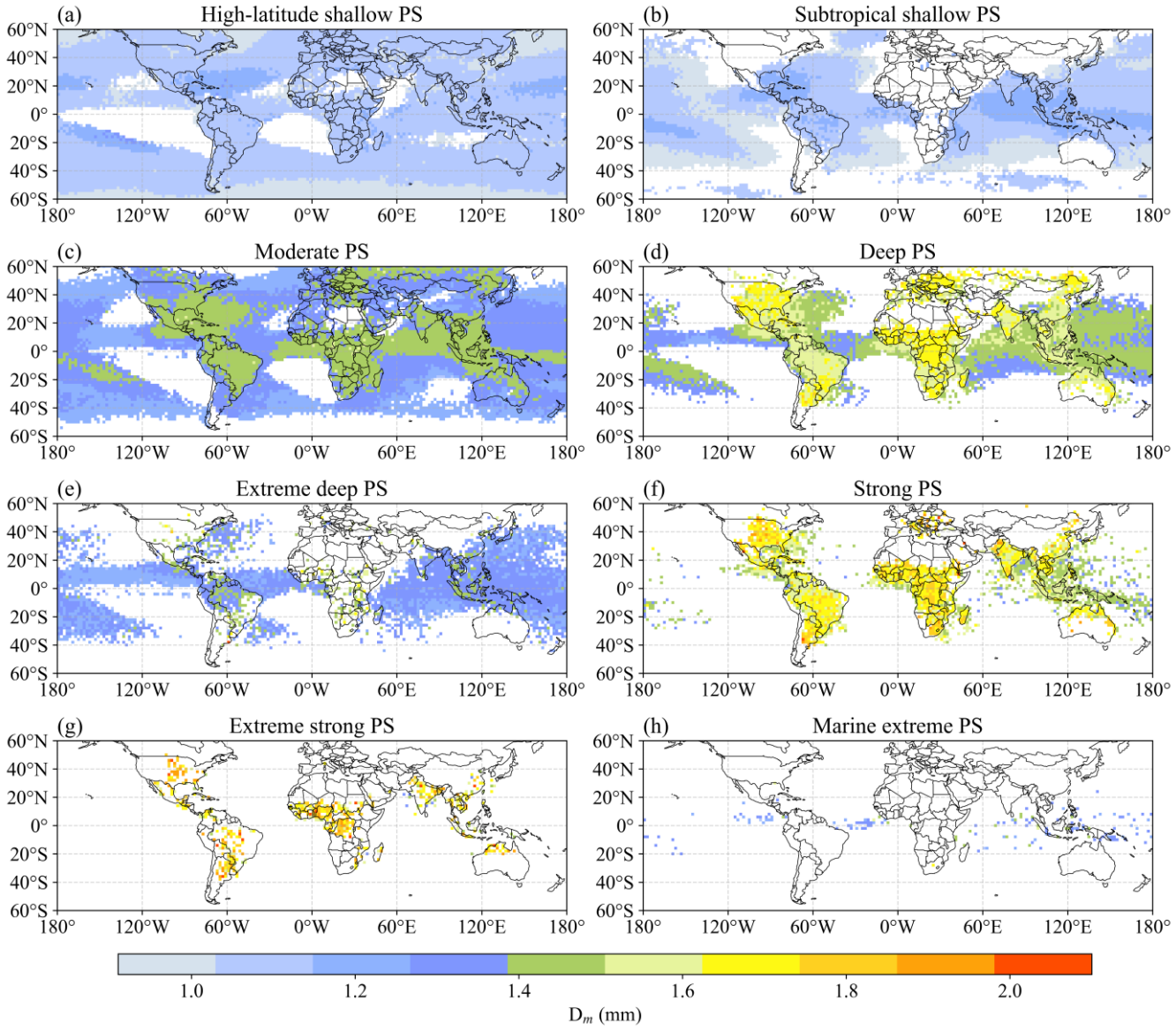

311

312 **Figure 2.** Spatial distributions of the mass-weighted mean diameter (D_m) for the eight PS clusters at a height of 2.5 km.

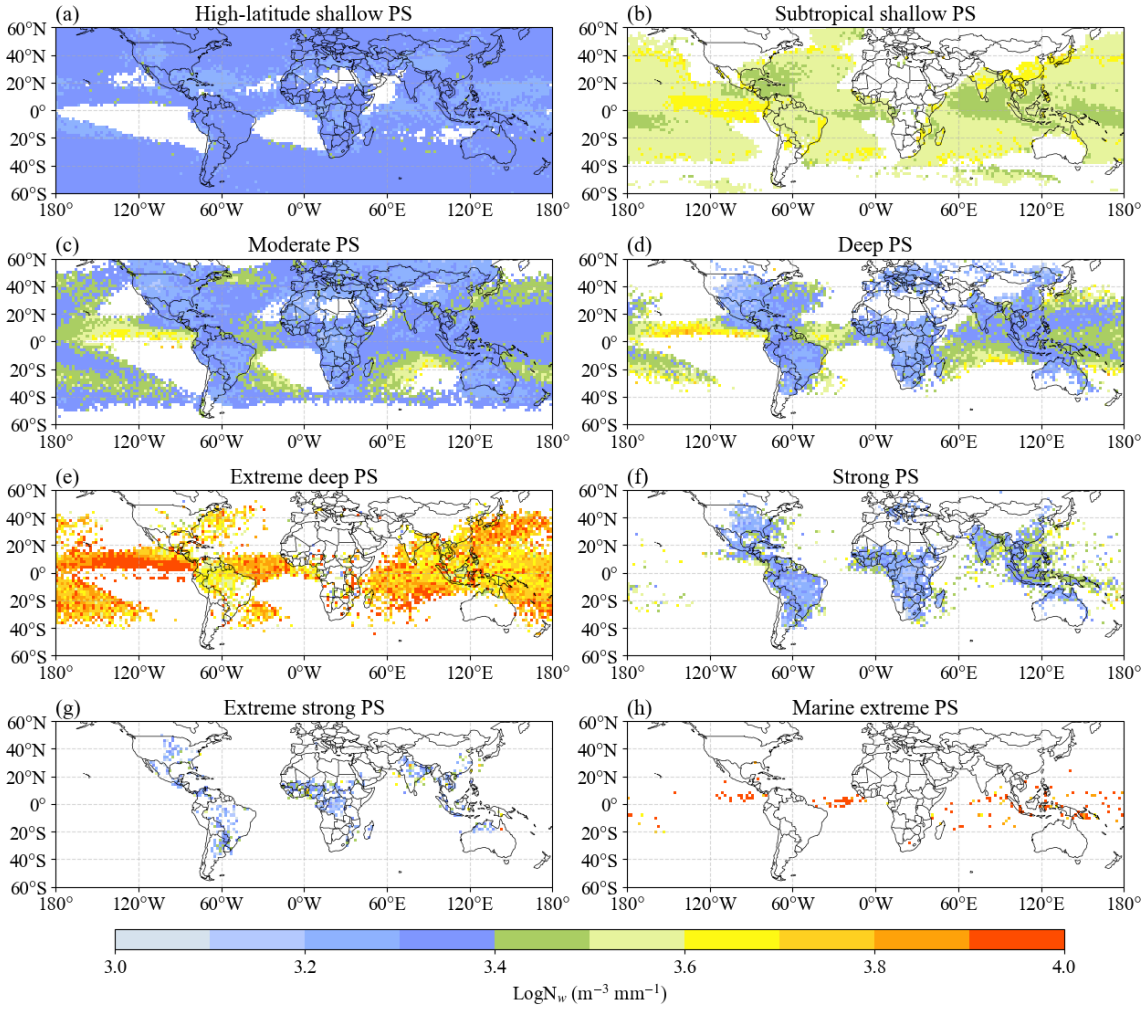

Figure 3. Similar to Fig. 2**.** but for log10(N_w).

3.3. Vertical structure of the different PS types

The contoured frequency by altitude diagrams (CFADs) of $D_{m,}$ N_w, and the maximum radar reflectivity for the eight clusters are shown in Fig. 4/5/6. Figure 4 shows the CFAD of the maximum radar reflectivity profiles. The results revealed high echo tops for deep PS, extreme deep PS, strong PS, and extreme strong PS, and low echo tops for high-latitude shallow PS and subtropical shallow PS. Extreme strong PS attained an echo top height greater than 18 km, and it also exhibited the strongest convection at the middle level. Its geographic distribution was exclusively terrestrial, which is consistent with other studies concluding that deep convective cores occur mostly over land (Houze Jr. et al., 2015). Extreme deep PS and marine extreme PS exhibited sharper decreasing trends from 6–12 km than extreme strong PS, indicating weaker convective updrafts. In contrast, extreme strong PS had stronger updrafts, producing more supercooled liquid droplets and large ice–water vapor

condensates (Jiang, 2012). In contrast, extreme deep PS and marine extreme PS showed lower 40 dBZ echo tops and a more rapid decrease in reflectivity above the freezing level. This suggests relatively weaker mid- and upper-level updrafts, which limit the vertical transport of ice particles and reduce the abundance of supercooled liquid and large condensate.

Table 2 indicates that the land proportion of extreme strong PS was much greater than that of extreme deep PS and marine extreme PS. Additionally, compared with oceanic environments, land land regions are generally characterized by relatively drier conditions and lapse rates closer to the dry adiabatic profile, which enhance buoyancy and allow stronger updrafts to loft ice crystals to higher altitudes. As a result, the maximum radar reflectivity in the middle levels at high altitudes decreased more slowly in extreme strong PS. High-latitude shallow PS and subtropical shallow PS yielded low echo tops of less than 6 km, indicating low convective intensity. Therefore, subtropical shallow PS could be identified as being associated with isolated shallow convection over the ocean, especially the region dominated by the subtropical high.

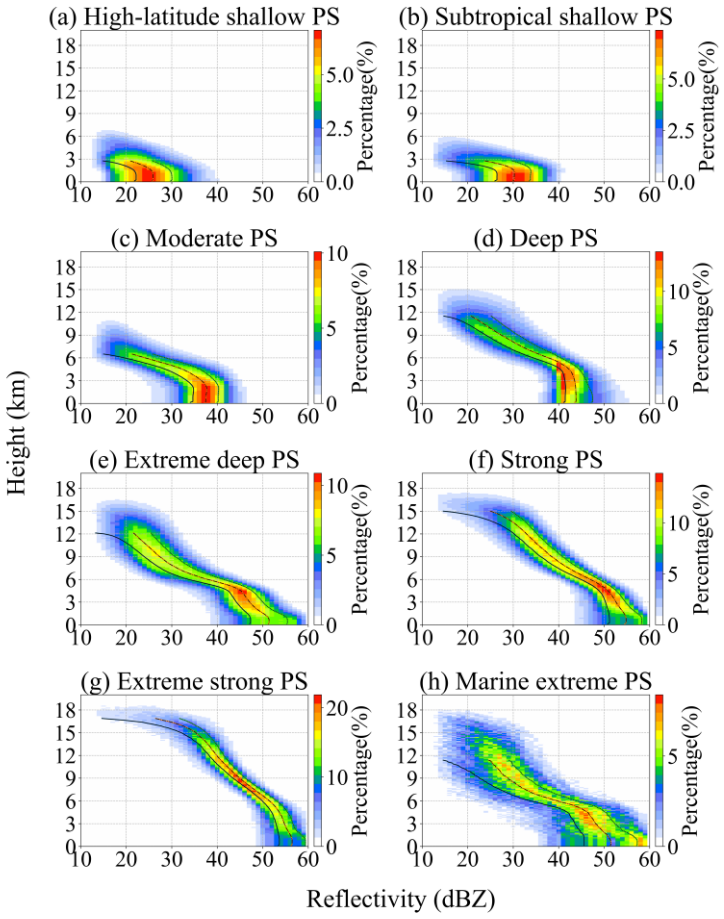

335

336 **Figure 4.** Contoured frequency by altitude diagrams (CFADs) of the maximum radar reflectivity for the eight distinct PS
337 clusters. The solid lines indicate the 25th percentiles; the dashed-dotted lines indicate the 50th percentiles; the dotted lines
338 indicate the 75th percentiles.

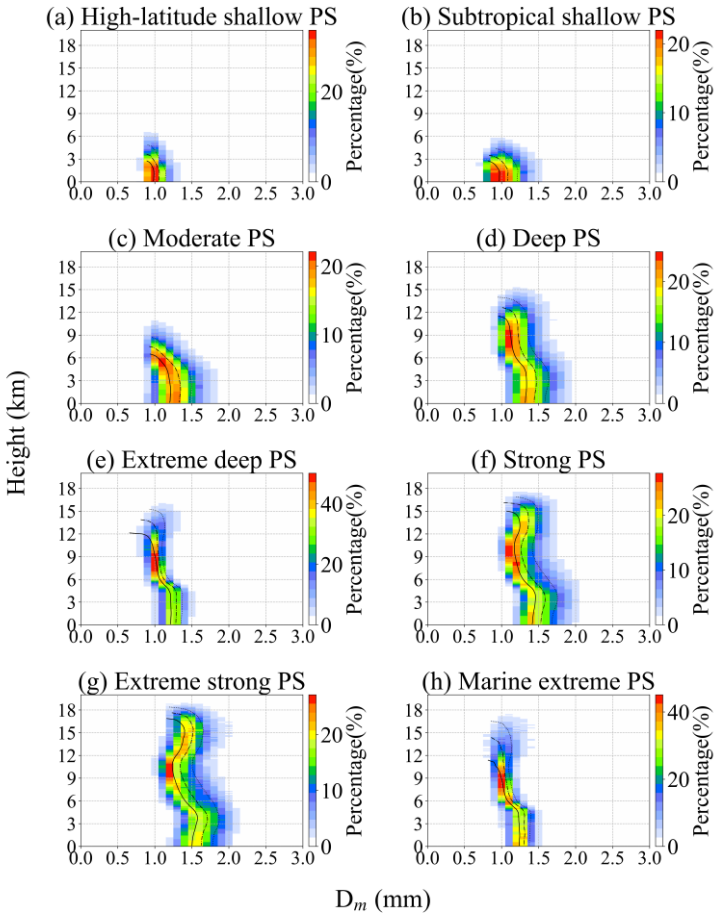

339

340 **Figure. 5.** Similar to Fig. 4, but for D_m.

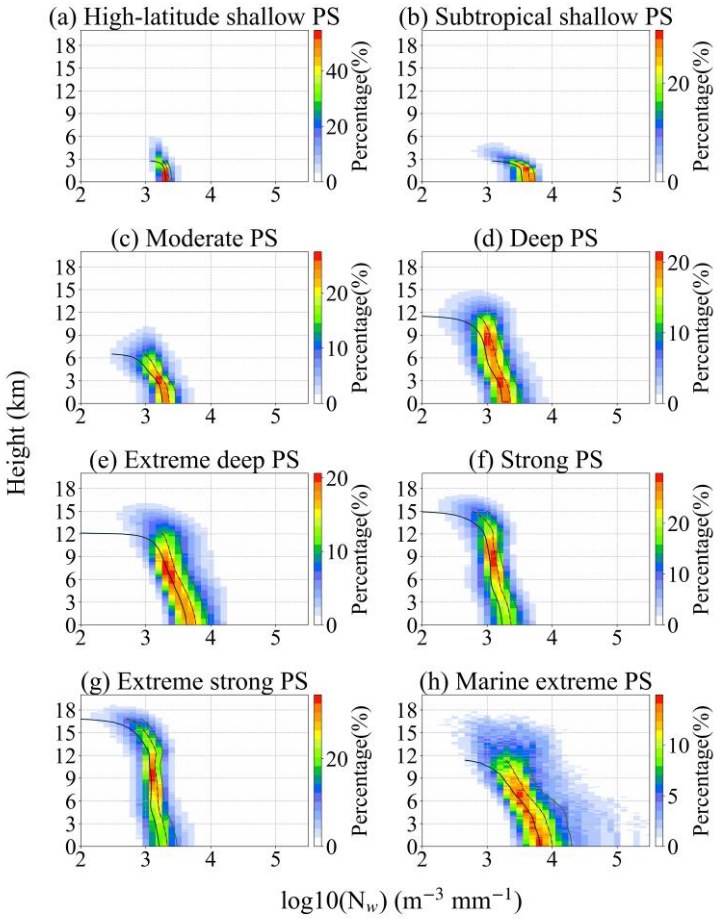

341

342 **Figure. 6.** Similar to Fig. 4, but for log10(N_w).

343 Figure 5 shows the CFAD of D_m for the eight types of PS. Generally, deep convections (deep PS, extreme deep PS, strong PS,
344 extreme strong PS, and marine extreme PS) produce different D_m values in the regions above and below approximately 5 km.
345 Moreover, strong PS and extreme strong PS exhibited wider distributions than those of extreme deep PS and marine extreme
346 PS. For deep PS, strong PS, and extreme strong PS, D_m below 4.8 km did not change much or slightly increased along with
347 height, but the value decreased between 4.8 and 6.9 km. In extreme strong PS, the vertical structure of D_m was more complex.
348 Extreme strong PS exhibited three regimes according to the variations in D_m. The first regime was observed between 0 and 4.1
349 km, where D_m increases with altitude. This is consistent with other papers involving the use of ground-based radar observations
350 and reporting that D_m of deep convective precipitation decreases with decreasing height near the surface (Marzuki et al., 2023).
351 The observed decrease in D_m may be related to the continued breakdown of large isolated raindrops in the atmosphere. The

second regime was observed above the freezing level, from 4.1 to 10 km, where D_m decreases with altitude. In this regime, the updraft in deep convection was decreased (Uma and Rao, 2009). The decline in updraft decreased the size of the particles that can be retained in the cloud. The rapid changes of D_m between the two regimes might be due to the changes of precipitation phase across the melting layer. As revealed by Mroz et al. (2024), the routine retrieval algorithm results in rapid changes of D_m and mass flux around the melting level, because the DPR observations cannot quantify ice water content and ice crystal size above the stratiform rain regions. Finally, the third regime was observed between 10 and 18 km, where D_m increases with altitude and where strengthened updrafts are often observed (Becker and Hohenegger, 2021). Although both high-latitude shallow PS and subtropical shallow PS were shallow PS, subtropical shallow PS had a wider distribution of D_m than high-latitude shallow PS. One possible reason is that in shallow oceanic convection, the breaking of large raindrops broadens the DSD.

Figure 6 shows the CFAD of log10(N_w) for the different types of PS. In general, N_w decreases with increasing altitude. The distribution range of N_w for shallow PS was relatively small. Moreover, the N_w distribution range of subtropical shallow PS was larger than that of high-latitude shallow PS. Among PS with intense convection, PS with a greater proportion of land coverage exhibited a narrower distribution of Nw, whereas PS with a greater proportion of ocean coverage exhibited higher N_w values. For example, the N_w values of strong PS and extreme strong PS were smaller and narrower than those of ocean-dominated deep PS, extreme deep PS and marine extreme PS. This finding is consistent with the conclusions of other studies (Kumar et al., 2024). One possible explanation is that the slower updrafts over ocean regions result in higher concentrations of smaller condensates at lower altitudes. Moreover, for both D_m and N_w, the four non-extreme PS exhibit little vertical variation below the melting layer, which may be attributed to a balance between coalescence and breakup processes.

3.4. DSD characteristics at a height of 2.5 km

Figure 7a-h show the frequency distributions of the mean D_m and log10(N_w) values observed at 2.5 km above ground level. The mean D_m values and the corresponding log10(N_w) values for the eight types of PS are detailed in Table 2. Generally, all the distributions shown in Fig. 7a-h greatly deviate from the parameters of continental convection and maritime convection defined by Bringi et al. (2003). One reason is that the mean values of D_m and N_w for one PS were considered here, whereas Bringi et al. (2003) separated the observation samples into stratiform and convective samples. Moreover, the DSDs observed by disdrometers are generally cumulative observations of a single storm at one fixed location and differ from the results for each PS in this study, which represent the instantaneous occurrence of a storm. With the most intense convection at the middle level, extreme strong PS was the closest to continental convection (Fig. 7d), whereas marine extreme PS was the closest to maritime convection (Fig. 7e). For most PS, D_m and N_w were negatively correlated, with greater dispersion of D_m than that of N_w. However, it should be noted that the observed correlations between D_m and N_w may partly be due to the retrieval assumptions in the GPM algorithm, which enforces a correlation between D_m and precipitation rate (Chase et al., 2020), rather

than purely physical relationships. Moreover, the shallow PS exhibited lower D_m and N_w values and narrower distributions than those of the deep PS.

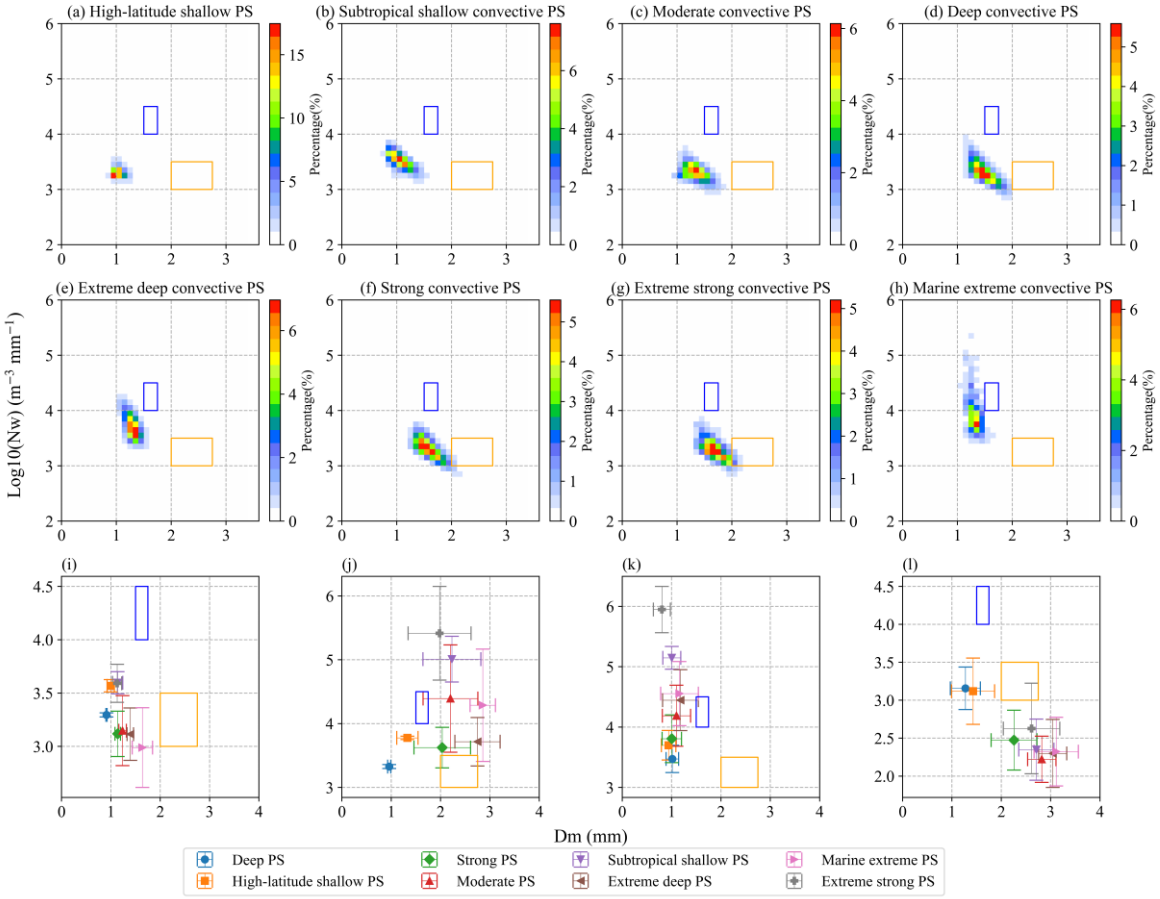

Figure 7. (a-h) Two-dimensional frequency distributions of D_m and log10(N_w) at a height of 2.5 km, and (i-l) statistical values of log10(N_w) and D_m for each PS (the bar indicates one standard deviation). (i) Mean values of D_m and log10(N_w), (j) MAX-D_m and MAX-log10(N_w), (k) MAX-log10(N_w) and D_m at its corresponding position, and (l) MAX-D_m and log10(N_w) at its corresponding position for each PS. The blue and orange rectangles denote the maritime and continental convective clusters, respectively, in D_m and log10(N_w) space from Bringi et al. (2003).

To further compare the mean D_m and N_w values of the different clusters, Figure 7i shows a summary of the mean D_m and N_w values, with the standard deviation for each type of PS. Marine extreme PS showed a significant abnormal low value of N_w, whereas the N_w value of extreme deep PS slightly deviated from those of the other PS. If only the three extreme deep PS with the highest echo tops (strong, extreme strong, and marine extreme PS) are considered, D_m and N_w show an inverse relationship.

These results might suggest that in deep convection, the DSD parameters at the near-surface level are related to convection intensity parameters. Ni et al. (2019) revealed that the dual-frequency ratio between the Ku and Ka bands at 12 km was positively correlated with intensity parameters such as MAXHT20/30, partly because stronger updrafts could hold larger ice particles in clouds.

Note that the mean D_m and N_w values do not capture the variety of DSDs in each PS. For example, the DSD might differ between convective and stratiform regions, where the N_w–D_m relationships might vary. To comprehensively demonstrate the microphysical features of PS, Figure 7j shows the mean MAX-D_m and MAX-N_w values of each PS at 2.5 km. For extreme PS, MAX-D_m and MAX-N_w were negatively correlated, while a positive correlation was observed for non-extreme PS. A similar relationship is also shown in Fig. 7k, which suggests a relationship between MAX-N_w and the corresponding D_m value in the MAX-N_w pixels of each PS. Nevertheless, as shown in Fig. 7k, the D_m values of all eight types of PS were very close. Nevertheless, it could be also found that in the non-extreme PS the D_m increases with MAX-N_w, while in the extreme PS, the D_m decreases with MAX-N_w. Figure 7l shows the relationship between MAX-D_m and the corresponding N_w value in the MAX-D_m pixels of each PS. Interestingly, for all eight types of PS, MAX-D_m and N_w showed significantly negative correlations. Note that MAX-D_m and MAX-N_w in Fig. 7j are the maximum values for one PS and usually do not occur in the same pixel. Figure 7k-l show the N_w–D_m relationship observed at the same location. Overall, the conclusions generally indicated that deep PS yield larger MAX-N_w or MAX-D_m values than shallow convection PS do. Overall, extreme PS exhibited negative correlations between N_w and D_m, whereas non-extreme PS demonstrated positive correlations.

In this study, we saw a positive relationship between the increase in D_m and MAXHT20 in extreme PS. However, extreme strong PS attained the highest MAXHT20 value, but its precipitation rate was lower than that of extreme deep PS and marine extreme PS. These results suggest a complex relationship between the microphysical parameters and convection features, especially in deep and intense convection systems. Notably, in extreme convection, intense precipitation at lower storm levels can cause significant rain-induced attenuation of the radar signal, which may in turn influence the retrieval accuracy of microphysical parameters. To assess the impact of attenuation on the D_m-N_w relationship, ground-based observations of microphysical properties from disdrometers are needed. Finally, we considered the PS as a whole. The microphysical characteristics varied among different pixels. The mean or maximum values of D_m and N_w only reflect part of the total process. Therefore, analyses on the basis of pixel-level observations would improve this work.

To gain further insight into the primary microphysical processes associated with the various PS, we employed an investigative approach analogous to that utilized by Kumjian and Prat (2014). To prevent the influence of ground-based clutter, ΔZ_e and ΔD_m values were calculated as the difference between Z_e and D_m at 2 and 3 km above the ground. Specifically, $\Delta Z_e = Z_e^{2km} - Z_e^{3km}$ and $\Delta D_m = D_m^{2km} - D_m^{3km}$ are calculated. Fig. 8 shows the frequency pattern of ΔZ_e versus ΔD_m for the eight types of PS. An increase (decrease) in Z_e and D_m indicates that coalescence (breakup) processes dominate. Balanced breakup and

coalescence processes result in an increase in Z_e but a decrease in D_m. In contrast, a decrease in Z_e and an increase in D_m are due to predominantly evaporation or size sorting processes (Wen et al., 2023).

The microphysical processes of the different types of PS exhibited clear differences. Notably, the microphysical processes were dominated by coalescence in the two types of shallow PS (Fig. 8a-b). Previous studies have demonstrated that high-latitude shallow PS are more likely to experience the condensation of rain droplets into snow due to the low temperatures in these regions (Thompson et al., 2015). Meanwhile, the coalescence process plays an important role in tropical oceanic shallow convective precipitation (subtropical shallow PS) as demonstrated by Li et al. (2024). Balanced breakup and coalescence processes in extreme PS accounted for more than 40% of the total microphysical processes, significantly exceeding the other three types of microphysical processes. The microphysical processes may reach an equilibrium state under high rainfall rates, in which the coalescence and breakup of raindrops are nearly balanced. These results are consistent with Shi et al. (2025), who found that extreme rainfall is primarily driven by vigorous mixed-phase processes and a balance between coalescence and breakup in liquid-phase processes. Extreme deep PS and marine extreme PS encompassed a higher percentage of coalescence processes than strong PS and extreme strong PS did, whereas strong PS and extreme strong PS encompassed a higher percentage of breakup processes.

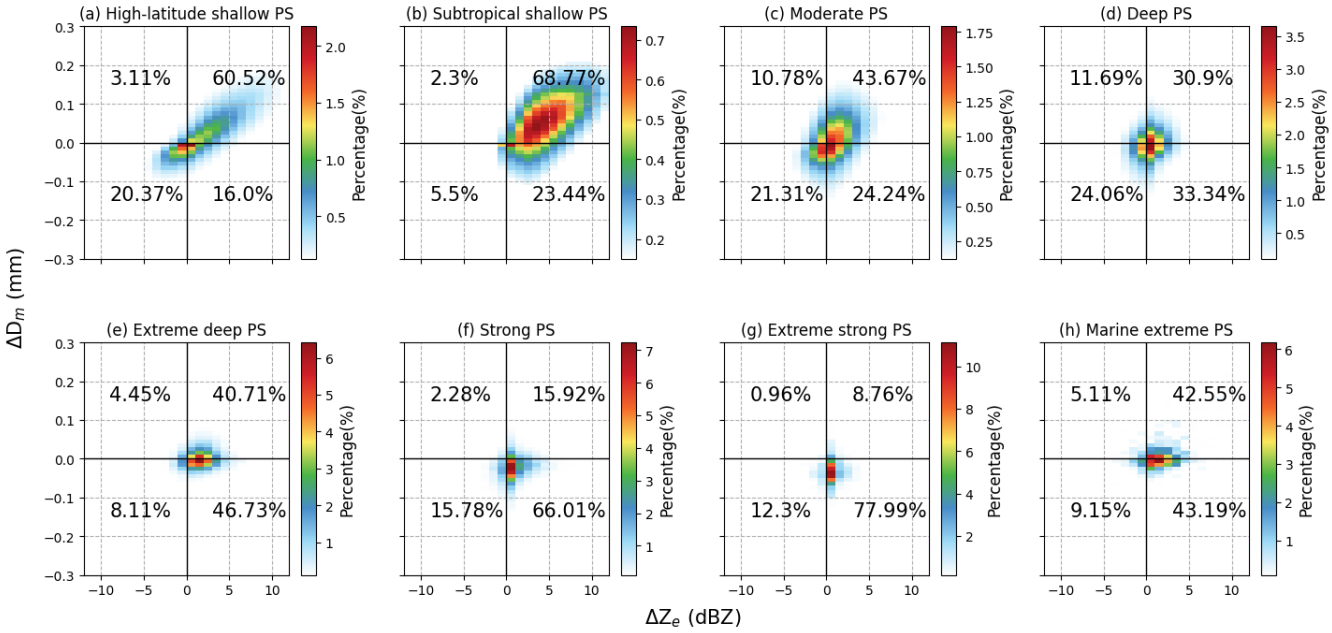

Figure 8. Frequency pattern of ΔZ_e versus ΔD_m between 2 and 3 km for the eight PS clusters.

3.5. Seasonal and diurnal cycles

In this study, seasons were categorized by fixed calendar months. The Northern Hemisphere seasons were defined as spring (March–May), summer (June–August), autumn (September–November), and winter (December–February). Conversely, the Southern Hemisphere seasons followed the opposite pattern: spring (September–November), summer (December–February), autumn (March–May), and winter (June–August). Based on this classification, the subsequent analysis examines seasonal and diurnal variations in PS frequency and microphysical parameters. Figure 9 shows the cycles of PS occurrence. Overall, the seasonal and diurnal cycles differed among the eight types of PS. Moderate PS, deep PS, strong PS, and extreme strong PS exhibited cycles like those of continental convection systems, with peaks in the afternoon and in summer. Dominated by tropical shallow convection over the ocean (Fig. 1**)**, subtropical shallow PS occurred mostly between 00:00 and 05:00 local time. and was more frequent during the autumn season than during the other seasons, with the lowest occurrence during the spring season. The other types of PS (high-latitude shallow PS, extreme deep PS, and marine extreme PS) did not show obvious diurnal cycles, except that high-latitude shallow PS indicated a low peak at approximately 6 am in winter and a valley before noon in summer. High-latitude shallow PS occurred infrequently in winter. Extreme deep PS occurred more frequently in summer and autumn, with fewer occurrences in winter. Note that marine extreme PS did not demonstrate obvious seasonal discrepancies, but showed a peak at night in the summer. Specifically, strong PS and extreme strong PS with a higher proportion over land exhibit a peak occurrence around 3 p.m. in the afternoon. In contrast, extreme deep PS and marine extreme PS mostly show no distinct peak, with frequencies distributed evenly throughout the day. This difference reflects the land-ocean contrast in extreme PS, which is consistent with findings from other related studies (Wang and Tang, 2020).

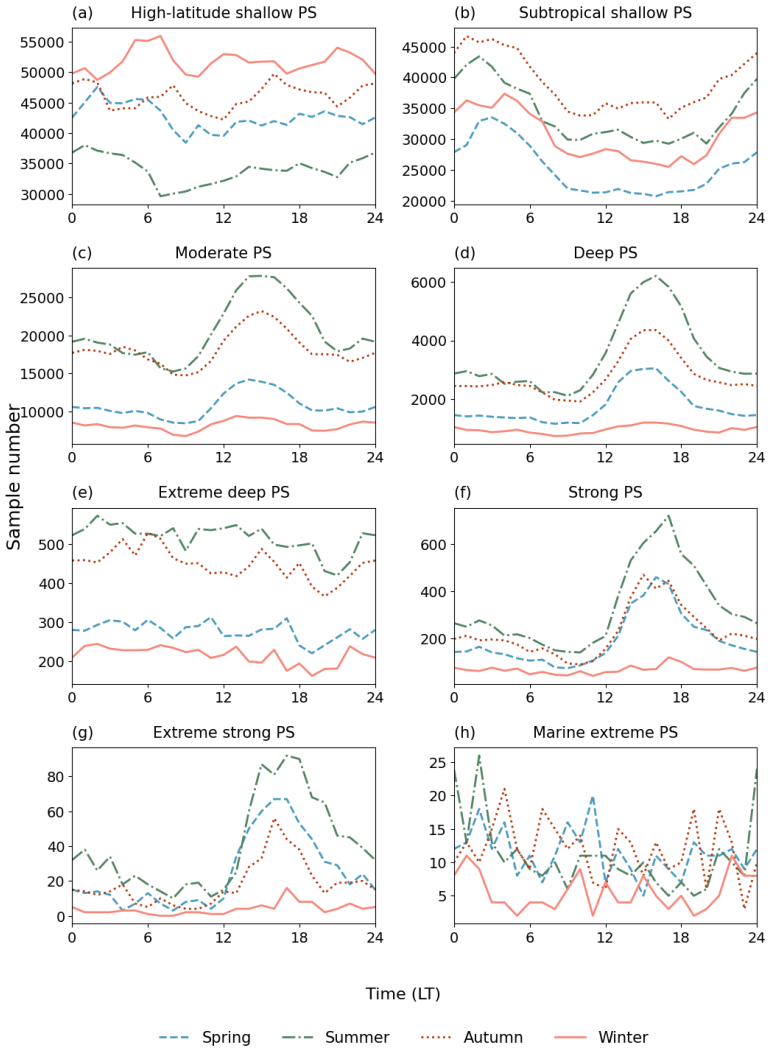

Figure 9. Diurnal variations in the sample sizes of the eight distinct PS clusters across the four seasons.

Figures 10 and 11 show the seasonal and diurnal cycles of D_m and N_w, respectively. The diurnal cycles of D_m were similar with those of PS occurrence to some extent. For example, in moderate PS, deep PS and strong PS, both the occurrence and D_m have peaks around 15 pm. One connection between these two parameters is that environments that favor storm occurrence could also facilitate the development of stronger updrafts, which could promote the formation of large particles in clouds. Nevertheless, discrepancies are obvious between the cycles of occurrence and D_m. For example, the D_m in the extreme strong PS did not show obvious diurnal variations. The high-latitude shallow PS shows a peak in the summer (Fig. 10a), which is not found in the diurnal cycle of occurrence (Fig. 9a). In subtropical shallow PS, the diurnal cycle of D_m (Fig. 10b) was the opposite to that of PS occurrence (Fig. 9b). The diurnal variation of N_w differed substantially from that of D_m and occurrence frequency. In subtropical shallow PS, moderate PS, deep PS, and strong PS, the N_w peaked in the morning. Nevertheless, the diurnal

cycles of subtropical shallow PS, moderate PS, and deep PS also differed. For example, N_w of subtropical shallow PS at night was low, whereas N_w of shallow convective PS and moderate PS at night was very close to its peak. Extreme deep PS and marine extreme PS did not exhibit obvious diurnal cycles of N_w. The extreme strong PS showed low values of N_w in the afternoon and little variation at night. For high-latitude shallow PS, diurnal variation is not clear except in the summer when the N_w in the afternoon is the lowest.

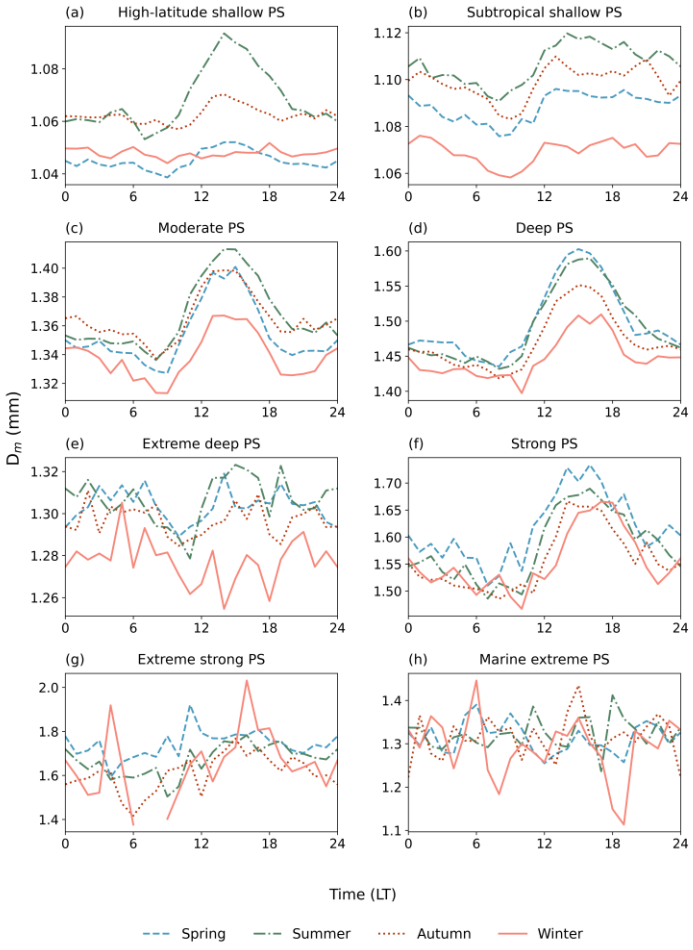

Figure 10. Similar to Fig. 9 but for mean D_m value.

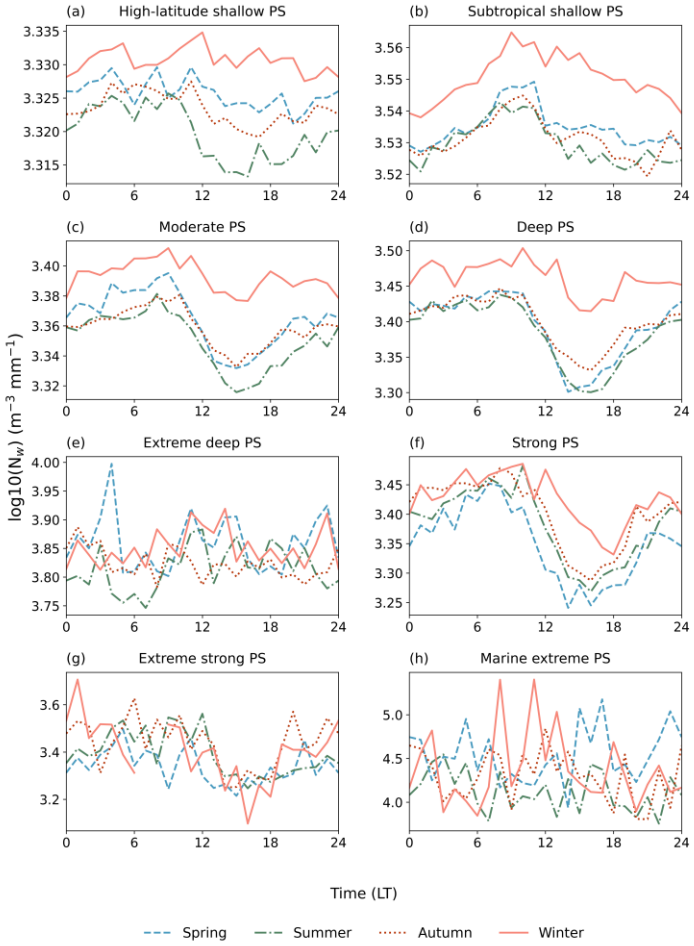

Figure 11. Similar to Fig. 9 but for the mean log10(N_w) value.

Similar to the diurnal cycles, the annual cycles of D_m and N_w were opposite in subtropical shallow PS, moderate PS, and deep PS, of which D_m was the lowest and N_w was the largest in winter. Nevertheless, there were also differences in the annual cycles of the three types of PS. For example, in subtropical shallow PS, D_m was the largest in summer, followed by autumn and spring, whereas the N_w values during the three seasons were very close. Among the extreme PS, N_w and D_m did not exhibit obvious annual cycles. For high-latitude shallow PS, the highest D_m value occurs in summer and the D_m in winter and spring were comparable. However, the annual cycle of N_w attained the largest value in winter and the lowest value in summer.

4. Conclusions

In this study, GPM DPR data were used to objectively classify global PS and analyze the microphysical characteristics of the different types of PS. The main conclusions are as follows:

1). By conducting an objective classification of global PS via key parameters such as the convective intensity, radar reflectivity, and DSD parameters, eight distinct types of PS were identified. These systems were classified on the basis of their unique microphysical and convective properties, providing a detailed understanding of the different precipitation processes worldwide. The eight types of PS identified are as four types of regular/non-extreme PS (high-latitude shallow PS, subtropical shallow PS, moderate PS, deep PS) and four types of extreme PS (extreme deep PS, strong PS, extreme strong PS, marine extreme PS).

2). MAXHT20 is generally correlated with the precipitation rate, but this relationship is not clear for extreme PS. The relationship between MAXHT20 and D_m does not follow a simple linear pattern. For extreme PS, MAXHT20 is positively related to D_m at 2.5 km above the ground surface. This may reflect the relationship between higher cloud tops and greater liquid water contents in strongly convective PS. However, for non-extreme PS, the relationship between MAXHT20 and D_m is more complex and may be influenced by variations in the physical processes of the different PS.

3). For the same type of PS, D_m over land is greater than that over the ocean. Additionally, D_m exhibits latitudinal variability, particularly in high-latitude shallow PS, where D_m decreases with increasing latitude. Additionally, continental rainfall is often associated with lower N_w values due to the dominance of the cold-rain (ice-phase) process, in which precipitation particles grow through riming and aggregation above the freezing level, typically producing larger but fewer drops after melting. In contrast, oceanic rainfall is more frequently governed by the warm-rain process dominated by collision–coalescence below the freezing level, which tends to generate more numerous but smaller raindrops and thus higher N_w values. Shallow PS generally exhibit narrow distributions of both D_m and N_w, particularly in high-latitude shallow PS. Among the strong PS, those with a higher land proportion exhibit a narrower distribution of Nw values, whereas those with a greater ocean proportion exhibit larger Nw values. However, the behavior of Dm is opposite: PS with a higher ocean proportion show a narrower distribution of Dm values than land-dominated PS.

4). The different PS exhibit distinct microphysical processes. In shallow convective PS, such as subtropical shallow PS and high-latitude shallow PS, coalescence processes largely shape the microphysical characteristics, indicating the aggregation of small raindrops in these PS. In contrast, extreme PS are characterized by balanced breakup and coalescence processes, highlighting a more complex interaction between raindrop formation and breakup. These results emphasize the varying mechanisms that govern microphysical behavior across the different types of PS. PS types with high precipitation rates are

dominated primarily by balanced breakup and coalescence processes, whereas shallow PS are characterized mainly by coalescence.

5). The seasonal and diurnal cycles of PS and their microphysical parameters vary across clusters. Continental convection clusters peak in the afternoon and summer, whereas tropical and high-latitude systems exhibit unique seasonal and diurnal cycles, often with opposite trends between D_m and N_w.

Classifying PS is essential for increasing the understanding of the microphysical processes that govern cloud development and precipitation formation across various climatic regimes. This classification enables the identification of key mechanisms that shape precipitation particle formation, growth, and distribution, thereby providing a more physically grounded view of precipitation system diversity. This study revealed the global distribution characteristics of different types of PS and elucidated the variations in microphysical properties across regions with distinct climatic and geographic conditions. Among the findings, the identified PS types are closely linked to consistent variations in key microphysical parameters, suggesting that this objective classification framework can effectively distinguish precipitation regimes with different underlying physical mechanisms. These results provide new observational evidence for global precipitation variability and establish a physically consistent framework for process-oriented comparisons, cross-regional analyses, and the evaluation of satellite precipitation products and numerical model representations of precipitation systems.

Data Availability. The GPM-DPR (version 07A) data from the NASA/Goddard Space Flight Center are available at https://disc.gsfc.nasa.gov/datasets/GPM_2A-DPR_07/summary. All statistics and visualization are operated with Anaconda Individual Edition Python version 3.8.3 (Free Download | Anaconda, accessed on 10 April 2022).

Author contributions. XZ and XN conceptualised and planned the research study. XZ conducted the satellite data analysis with support from XN and drafted the initial manuscript. XN and JZ reviewed and revised the manuscript to refine its content.

Competing interests. The contact author has declared that none of the authors has any competing interests.

Financial support. This study is supported by the National Natural Science Foundation of China (42105005), Fundamental Research Funds for the Central Universities (SWU-KT22007), and General Program of Chongqing Natural Science Foundation (2022NSCQ-MSX3145).

References

Arulraj, M. and Barros, A. P.: Automatic detection and classification of low-level orographic precipitation processes from space-borne radars using machine learning, Remote Sensing of Environment, 257, 112355, https://doi.org/10.1016/j.rse.2021.112355, 2021.

Awaka, J., Le, M., Brodzik, S., Kubota, T., Masaki, T., Chandrasekar, V., and Iguchi, T.: Development of precipitation type classification algorithms for a full scan mode of GPM dual-frequency precipitation radar, Journal of the Meteorological Society of Japan. Ser. II, 99, 1253–1270, https://doi.org/10.2151/jmsj.2021-061, 2021.

Ay, M., Özbakır, L., Kulluk, S., Gülmez, B., Öztürk, G., and Özer, S.: FC-Kmeans: Fixed-centered K-means algorithm, Expert Systems with Applications, 211, 118656, https://doi.org/10.1016/j.eswa.2022.118656, 2023.

Bang, S. D. and Cecil, D. J.: Testing Passive Microwave-Based Hail Retrievals Using GPM DPR Ku-Band Radar, Journal of Applied Meteorology and Climatology, 60, 255–271, https://doi.org/10.1175/JAMC-D-20-0129.1, 2021.

Becker, T. and Hohenegger, C.: Entrainment and its dependency on environmental conditions and convective organization in convection-permitting simulations, Monthly Weather Review, 149, 537–550, https://doi.org/10.1175/MWR-D-20-0229.1, 2021.

Bringi, V. N., Chandrasekar, V., Hubbert, J., Gorgucci, E., Randeu, W. L., and Schoenhuber, M.: Raindrop size distribution in different climatic regimes from disdrometer and dual-polarized radar analysis, Journal of the Atmospheric Sciences, 60, 354–365, https://doi.org/10.1175/1520-0469(2003)060<0354:RSDIDC>2.0.CO;2, 2003.

Cha, J. W. and Yum, S. S.: Characteristics of Precipitation Particles Measured by PARSIVEL Disdrometer at a Mountain and a Coastal Site in Korea, Asia-Pacific J Atmos Sci, 57, 261–276, https://doi.org/10.1007/s13143-020-00190-6, 2021.

Chase, R. J., Nesbitt, S. W., and McFarquhar, G. M.: Evaluation of the Microphysical Assumptions within GPM-DPR Using Ground-Based Observations of Rain and Snow, Atmosphere, 11, 619, https://doi.org/10.3390/atmos11060619, 2020.

Chen, B. and Liu, C.: Warm organized rain systems over the tropical eastern Pacific, Journal of Climate, 29, 3403–3422, https://doi.org/10.1175/JCLI-D-15-0177.1, 2016.

Chen, B., Hu, W., and Pu, J.: Characteristics of the raindrop size distribution for freezing precipitation observed in southern China, Journal of Geophysical Research: Atmospheres, 116, https://doi.org/10.1029/2010JD015305, 2011.

Chudler, K., Rutledge, S. A., and Dolan, B.: Unique radar observations of large raindrops in tropical warm rain during PISTON, Monthly Weather Review, 150, 2719–2736, https://doi.org/10.1175/MWR-D-21-0298.1, 2022.

D'Adderio, L. P., Vulpiani, G., Porcù, F., Tokay, A., and Meneghini, R.: Comparison of GPM Core Observatory and Ground-Based Radar Retrieval of Mass-Weighted Mean Raindrop Diameter at Midlatitude, Journal of Hydrometeorology, 19, 1583–1598, https://doi.org/10.1175/JHM-D-18-0002.1, 2018.

Dai, Q., Zhu, J., Zhang, S., Zhu, S., Han, D., and Lv, G.: Estimation of rainfall erosivity based on WRF-derived raindrop size distributions, Hydrology and Earth System Sciences, 24, 5407–5422, https://doi.org/10.5194/hess-24-5407-2020, 2020.

Das, S. and Chatterjee, C.: Rain characterization based on maritime and continental origin at a tropical location, Journal of Atmospheric and Solar-Terrestrial Physics, 173, 109–118, https://doi.org/10.1016/j.jastp.2018.02.011, 2018.

Das, S., Wang, Y., Gong, J., Ding, L., Munchak, S. J., Wang, C., Wu, D. L., Liao, L., Olson, W. S., and Barahona, D. O.: A comprehensive machine learning study to classify precipitation type over land from Global Precipitation Measurement Microwave Imager (GPM-GMI) measurements, Remote Sensing, 14, 3631, https://doi.org/10.3390/rs14153631, 2022.

Dolan, B., Fuchs, B., Rutledge, S. A., Barnes, E. A., and Thompson, E. J.: Primary modes of global drop size distributions, Journal of the Atmospheric Sciences, 75, 1453–1476, https://doi.org/10.1175/JAS-D-17-0242.1, 2018.

El Khattabi, M.-Z., El Jai, M., Lahmadi, Y., Oughdir, L., and Rahhali, M.: Understanding the Interplay Between Metrics, Normalization Forms, and Data distribution in K-Means Clustering: A Comparative Simulation Study, Arab J Sci Eng, 49, 2987–3007, https://doi.org/10.1007/s13369-023-07741-9, 2024.

Festa, D., Novellino, A., Hussain, E., Bateson, L., Casagli, N., Confuorto, P., Del Soldato, M., and Raspini, F.: Unsupervised detection of InSAR time series patterns based on PCA and K-means clustering, International Journal of Applied Earth Observation and Geoinformation, 118, 103276, https://doi.org/10.1016/j.jag.2023.103276, 2023.

Gang, A. and Bajwa, W. U.: FAST-PCA: A Fast and Exact Algorithm for Distributed Principal Component Analysis, IEEE Transactions on Signal Processing, 70, 6080–6095, https://doi.org/10.1109/TSP.2022.3229635, 2022.

Gatlin, P. N., Petersen, W. A., Pippitt, J. L., Berendes, T. A., Wolff, D. B., and Tokay, A.: The GPM Validation Network and Evaluation of Satellite-Based Retrievals of the Rain Drop Size Distribution, Atmosphere, 11, https://doi.org/10.3390/atmos11091010, 2020.

Gupta, A. K., Deshmukh, A., Waman, D., Patade, S., Jadav, A., Phillips, V. T. J., Bansemer, A., Martins, J. A., and Gonçalves, F. L. T.: The microphysics of the warm-rain and ice crystal processes of precipitation in simulated continental convective storms, Commun Earth Environ, 4, 226, https://doi.org/10.1038/s43247-023-00884-5, 2023.

Hamada, A., Takayabu, Y. N., Liu, C., and Zipser, E. J.: Weak linkage between the heaviest rainfall and tallest storms, Nature Communications, 6, 6213, https://doi.org/10.1038/ncomms7213, 2015.

Hou, A. Y., Kakar, R. K., Neeck, S., Azarbarzin, A. A., Kummerow, C. D., Kojima, M., Oki, R., Nakamura, K., and Iguchi, T.: The global precipitation measurement mission, Bulletin of the American Meteorological Society, 95, 701–722, https://doi.org/10.1175/BAMS-D-13-00164.1, 2014.

Houze Jr., R. A., Rasmussen, K. L., Zuluaga, M. D., and Brodzik, S. R.: The variable nature of convection in the tropics and subtropics: A legacy of 16 years of the Tropical Rainfall Measuring Mission satellite, Reviews of Geophysics, 53, 994–1021, https://doi.org/10.1002/2015RG000488, 2015.

Hu, X., Ai, W., Qiao, J., and Yan, W.: Insight into global climatology of melting layer: latitudinal dependence and orographic relief, Theor Appl Climatol, 155, 4863–4873, https://doi.org/10.1007/s00704-024-04926-6, 2024.

Huang, H., Zhao, K., Fu, P., Chen, H., Chen, G., and Zhang, Y.: Validation of Precipitation Measurements From the Dual-Frequency Precipitation Radar Onboard the GPM Core Observatory Using a Polarimetric Radar in South China, IEEE Transactions on Geoscience and Remote Sensing, 60, 1–16, https://doi.org/10.1109/TGRS.2021.3118601, 2022.

Iguchi, T., Kozu, T., Meneghini, R., Awaka, J., and Okamoto, K.: Rain-Profiling algorithm for the TRMM precipitation radar, Journal of Applied Meteorology and Climatology, 39, 2038–2052, https://doi.org/10.1175/1520-0450(2001)040<2038:RPAFTT>2.0.CO;2, 2000.

Iguchi, T., Seto, S., Meneghini, R., Yoshida, N., Awaka, J., Le, M., Chandrasekar, V., Brodzik, S., Tanelli, S., Kanemaru, K., Masaki, T., Kubota, T., and Takahashi, N.: GPM/DPR Level-2 Algorithm Theoretical Basis Document, 2021.

Jain, A. K.: Data clustering: 50 years beyond K-means, Pattern Recognition Letters, 31, 651–666, https://doi.org/10.1016/j.patrec.2009.09.011, 2010.

Jiang, H.: The relationship between tropical cyclone intensity change and the strength of inner-core convection, Monthly Weather Review, 140, 1164–1176, https://doi.org/10.1175/MWR-D-11-00134.1, 2012.

Jolliffe, I. T. and Cadima, J.: Principal component analysis: a review and recent developments, Philosophical Transactions of the Royal Society A: Mathematical, Physical and Engineering Sciences, 374, 20150202, https://doi.org/10.1098/rsta.2015.0202, 2016.

Kumar, K. S., Das, S. K., Deshpande, S. M., Deshpande, M., and Pandithurai, G.: Regional variability of precipitation characteristics in tropical cyclones over the North Indian Ocean from GPM-DPR measurements, Atmospheric Research, 283, 106568, https://doi.org/10.1016/j.atmosres.2022.106568, 2023.

Kumar, S., Flores-Rojas, J. L., Moya-Álvarez, A. S., Martínez-Castro, D., and Silva, Y.: Hydrometeors distribution in intense precipitating cloud cells over the earth's during two rainfall seasons, J Indian Soc Remote Sens, 52, 95–111, https://doi.org/10.1007/s12524-023-01805-x, 2024.

Kumjian, M. R. and Prat, O. P.: The impact of raindrop collisional processes on the polarimetric radar variables, Journal of the Atmospheric Sciences, 71, 3052–3067, https://doi.org/10.1175/JAS-D-13-0357.1, 2014.

Lerber, A. von, Moisseev, D., Marks, D. A., Petersen, W., Harri, A.-M., and Chandrasekar, V.: Validation of GMI Snowfall Observations by Using a Combination of Weather Radar and Surface Measurements, Journal of Applied Meteorology and Climatology, 57, 797–820, https://doi.org/10.1175/JAMC-D-17-0176.1, 2018.

Li, D., Qi, Y., and Li, H.: Statistical characteristics of convective and stratiform precipitation during the rainy season over South China based on GPM-DPR observations, Atmospheric Research, 301, 107267, https://doi.org/10.1016/j.atmosres.2024.107267, 2024.

Liu, C.: Rainfall Contributions from Precipitation Systems with Different Sizes, Convective Intensities, and Durations over the Tropics and Subtropics, Journal of Hydrometeorology, 12, 394–412, https://doi.org/10.1175/2010JHM1320.1, 2011.

Liu, C. and Zipser, E. J.: The global distribution of largest, deepest, and most intense precipitation systems, Geophysical Research Letters, 42, 3591–3595, https://doi.org/10.1002/2015GL063776, 2015.

Liu, C., Zipser, E. J., and Nesbitt, S. W.: Global Distribution of Tropical Deep Convection: Different Perspectives from TRMM Infrared and Radar Data, https://doi.org/10.1175/JCLI4023.1, 2007.

Liu, C., Zipser, E. J., Cecil, D. J., Nesbitt, S. W., and Sherwood, S.: A cloud and precipitation feature database from nine years of TRMM observations, Journal of Applied Meteorology and Climatology, 47, 2712–2728, https://doi.org/10.1175/2008JAMC1890.1, 2008.

Liu, N., Liu, C., and Hayden, L.: Climatology and detection of overshooting convection from 4 years of GPM precipitation radar and passive microwave observations, Journal of Geophysical Research: Atmospheres, 125, e2019JD032003, https://doi.org/10.1029/2019JD032003, 2020.

Marukatat, S.: Tutorial on PCA and approximate PCA and approximate kernel PCA, Artif Intell Rev, 56, 5445–5477, https://doi.org/10.1007/s10462-022-10297-z, 2023.

Marzuki, M., Ramadhan, R., Yusnaini, H., Renggono, F., Vonnisa, M., and Hashiguchi, H.: Comparison of vertical profile of raindrop size distribution from micro rain radar with global precipitation measurement over Western Java Island, Remote Sensing Applications: Society and Environment, 29, 100885, https://doi.org/10.1016/j.rsase.2022.100885, 2023.

Mroz, K., Battaglia, A., and Fridlind, A. M.: Enhancing consistency of microphysical properties of precipitation across the melting layer in dual-frequency precipitation radar data, Atmospheric Measurement Techniques, 17, 1577–1597, https://doi.org/10.5194/amt-17-1577-2024, 2024.

Ni, X., Liu, C., Cecil, D. J., and Zhang, Q.: On the detection of hail Using satellite passive microwave radiometers and precipitation radar, Journal of Applied Meteorology and Climatology, 56, 2693–2709, https://doi.org/10.1175/JAMC-D-17-0065.1, 2017.

Ni, X., Liu, C., and Zipser, E.: Ice microphysical properties near the tops of deep convective cores implied by the GPM Dual-Frequency Radar observations, Journal of the Atmospheric Sciences, 76, 2899–2917, https://doi.org/10.1175/JAS-D-18-0243.1, 2019.

Peinó, E., Bech, J., Polls, F., Udina, M., Petracca, M., Adirosi, E., Gonzalez, S., and Boudevillain, B.: Validation of GPM DPR Rainfall and Drop Size Distributions Using Disdrometer Observations in the Western Mediterranean, Remote Sensing, 16, 2594, https://doi.org/10.3390/rs16142594, 2024.

Roy, P., Biswasharma, R., Deshamukhya, A., and Sharma, S.: Spatial and seasonal variation of rainfall contribution by the height spectrum of precipitation systems and associated cloud bulk properties over the South Asia, International Journal of Climatology, 40, 3771–3791, https://doi.org/10.1002/joc.6427, 2020.

Saha, P., Majumder, S., and Maitra, A.: Rain drop size distribution analysis at a tropical location near land-sea boundary, Theor Appl Climatol, 147, 487–498, https://doi.org/10.1007/s00704-021-03809-4, 2022.

Seela, B. K., Janapati, J., Lin, P.-L., Wang, P. K., and Lee, M.-T.: Raindrop size distribution characteristics of summer and winter season rainfall over North Taiwan, Journal of Geophysical Research: Atmospheres, 123, 11,602-11,624, https://doi.org/10.1029/2018JD028307, 2018.

Seela, B. K., Janapati, J., Lin, P.-L., Lan, C.-H., and Huang, M.-Q.: Evaluation of GPM DPR Rain Parameters with North Taiwan Disdrometers, https://doi.org/10.1175/JHM-D-23-0027.1, 2023.

690 Shi, R., Lu, C., Xu, W., and Luo, Y.: A global view on microphysical discriminations between heavier and lighter convective
691 rainfall, Commun Earth Environ, 6, 511, https://doi.org/10.1038/s43247-025-02473-0, 2025.
692 Skofronick-Jackson, G., Petersen, W. A., Berg, W., Kidd, C., Stocker, E. F., Kirschbaum, D. B., Kakar, R., Braun, S. A.,
693 Huffman, G. J., Iguchi, T., Kirstetter, P. E., Kummerow, C., Meneghini, R., Oki, R., Olson, W. S., Takayabu, Y. N., Furukawa,
694 K., and Wilheit, T.: The global precipitation measurement (GPM) mission for science and society, Bulletin of the American
695 Meteorological Society, 98, 1679–1695, https://doi.org/10.1175/BAMS-D-15-00306.1, 2017.
696 Snook, N. and Xue, M.: Effects of microphysical drop size distribution on tornadogenesis in supercell thunderstorms,
697 Geophysical Research Letters, 35, https://doi.org/10.1029/2008GL035866, 2008.
698 Sowan, B., Hong, T.-P., Al-Qerem, A., Alauthman, M., and Matar, N.: Ensembling validation indices to estimate the optimal
699 number of clusters, Appl Intell, 53, 9933–9957, https://doi.org/10.1007/s10489-022-03939-w, 2023.
700 Suh, S.-H., You, C.-H., and Lee, D.-I.: Climatological characteristics of raindrop size distributions in Busan, Republic of Korea,
701 Hydrology and Earth System Sciences, 20, 193–207, https://doi.org/10.5194/hess-20-193-2016, 2016.
702 Sun, Y., Dong, X., Cui, W., Zhou, Z., Fu, Z., Zhou, L., Deng, Y., and Cui, C.: Vertical Structures of Typical Meiyu
703 Precipitation Events Retrieved From GPM-DPR, Journal of Geophysical Research: Atmospheres, 125, e2019JD031466,
704 https://doi.org/10.1029/2019JD031466, 2020.
705 Tapiador, F. J., Turk, F. J., Petersen, W., Hou, A. Y., García-Ortega, E., Machado, L. A. T., Angelis, C. F., Salio, P., Kidd, C.,
706 Huffman, G. J., and de Castro, M.: Global precipitation measurement: Methods, datasets and applications, Atmospheric
707 Research, 104–105, 70–97, https://doi.org/10.1016/j.atmosres.2011.10.021, 2012.
708 Thompson, E. J., Rutledge, S. A., Dolan, B., and Thurai, M.: Drop size distributions and radar observations of convective and
709 stratiform rain over the equatorial Indian and west Pacific Oceans, Journal of the Atmospheric Sciences, 72, 4091–4125,
710 https://doi.org/10.1175/JAS-D-14-0206.1, 2015.
711 Uma, K. N. and Rao, T. N.: Characteristics of vertical velocity cores in different convective systems observed over Gadanki,
712 India, Monthly Weather Review, 137, 954–975, https://doi.org/10.1175/2008MWR2677.1, 2009.
713 Wang, T. and Tang, G.: Spatial Variability and Linkage Between Extreme Convections and Extreme Precipitation Revealed
714 by 22-Year Space-Borne Precipitation Radar Data, Geophysical Research Letters, 47, e2020GL088437,
715 https://doi.org/10.1029/2020GL088437, 2020.
716 Wen, J., Wang, G., Zhou, R., Li, R., Zhaxi, S., and Bai, M.: Seasonal Variation in Vertical Structure for Stratiform Rain at
717 Mêdog Site in Southeastern Tibetan Plateau, Remote Sensing, 16, 1230, https://doi.org/10.3390/rs16071230, 2024.
718 Wen, L., Chen, G., Yang, C., Zhang, H., and Fu, Z.: Seasonal variations in precipitation microphysics over East China based
719 on GPM DPR observations, Atmospheric Research, 293, 106933, https://doi.org/10.1016/j.atmosres.2023.106933, 2023.
720 Wu, Z., Zhang, Y., Zhang, L., Zheng, H., and Huang, X.: A comparison of convective and stratiform precipitation microphysics
721 of the record-breaking typhoon In-Fa (2021), Remote Sensing, 14, 344, https://doi.org/10.3390/rs14020344, 2022.
722 Zhang, Y. and Wang, K.: Global precipitation system size, Environ. Res. Lett., 16, 054005, https://doi.org/10.1088/1748-
723 9326/abf394, 2021.

Zhang, Z., Li, H., Li, D., and Qi, Y.: Spatial variability of raindrop size distribution at Beijing city scale and its implications for polarimetric radar QPE, Remote Sensing, 15, 3964, https://doi.org/10.3390/rs15163964, 2023.

Zipser, E. J., Cecil, D. J., Liu, C., Nesbitt, S. W., and Yorty, D. P.: WHERE ARE THE MOST INTENSE THUNDERSTORMS ON EARTH?, Bull. Amer. Meteor. Soc., 87, 1057–1072, https://doi.org/10.1175/BAMS-87-8-1057, 2006.